Supersaturation-Controlled Growth of Monolithically Integrated Lead-Free Halide Perovskite Single-Crystalline Thin Film for High-Sensitivity Photodetectors

Ziqing Li, Xinya Liu, Chaolei Zuo, Wei Yang, and Xiaosheng Fang*

Monolithical integration of the promising optoelectronic material with mature and inexpensive silicon circuitry contributes to simplifying device geometry, enhancing performance, and expanding new functionalities. Herein, a lead-free halide perovskite $Cs_3Bi_2I_9$ single-crystalline thin film (SCTF), with thickness ranging from 900 nm to 4.1 μm and aspect ratio up to 1666, is directly integrated on various substrates including Si wafer, through a facile and low-temperature solution-processing method. The growth kinetics of the lead-free halide perovskite SCTF are elucidated by in situ observation, and the solution supersaturation is controlled to reduce the inverse-temperature crystallization nucleation density and elongate the evaporation growth. The excellent lattice match and band alignment between Si(111) and $Cs_3Bi_2I_9$(001) facets promote photogenerated charge dissociation and extraction, resulting in boosting the photoelectric sensitivity by 10–200 times compared with photodetectors based on other substrates. More importantly, this silicon-compatible perovskite SCTF photodetector exhibits a high switching ratio of 3000 and a fast response of 1.5 μs, which are higher than most reported state-of-the-art lead-free halide perovskite photodetectors. This work not only gives an in-depth understanding of the perovskite precursor solution chemistry, but also demonstrates the great potential of monolithical integration of lead-free halide perovskite SCTF with a silicon wafer for high-performance photodetectors.

1. Introduction

Lead-free halide perovskites, which are environmentally friendly in large-scale commercialization, have demonstrated attractive prospects for many optoelectronic fields including highly efficient solar cell,[1] light-emitting diode,[2] solid-state laser[3] and high-sensitivity photodetector,[4] owing to long carrier lifetime, high carrier mobility and large absorption coefficient. Although the lead-free halide perovskite has realized many achievements, it is worth mentioning that the performance is limited by the polycrystalline form.[5] Bulk lead-free halide perovskite single crystals exhibit much better stability, longer diffusion length,

higher carrier mobility and longer carrier lifetime, thanks to their fewer grain boundaries, enhanced crystallinity and reduced trap density. With such performance improvements, the lead-free halide perovskite single crystal is considered to be a promising photosensitive material in optoelectronic devices.[6]

In order to effectively promote power conversion efficiency, the thickness of lead-free halide perovskite single crystal should be controlled at a suitable level, which is suggested to be greater than light-absorption length and less than carrier-diffusion length.[7] In the current semiconductor and photoelectronic industries, thin silicon wafers are fabricated mainly through top-down process, which requires high yields accompanied with large material loss, waste and subsequent complicated slicing process. Against this background, a facile and effective space-confined fabrication is adopted to produce large single-crystalline thin film, through a bottom-up process.[8] Compared with vapor epitaxial growth and cavitation triggered asymmetrical crystallization,[9] space-confined methods possess moderate growth conditions to grow SCTF without rigorous restrictions. However, this method is limited to the growth of organic-inorganic lead halide perovskite SCTF, few studies focus on lead-free halide perovskite SCTF, such as Sn-based, Bi-based and Sb-based, etc. This is limited by the lack of understanding of the precursor solution chemistry in space-confined method.[10] Although previous work pointed out that the preheated-substrate and local heating are important in the space-confined growth,[11] there is a lack of investigation on the influence of the precursor solution temperature on the crystallization process. In general, the growth drive force of the space-confined growth is considered to be inverse-temperature crystallization or solvent evaporation, in which the supersaturation plays a key role in controlling size and quality.[12] An in-depth insight of the relationship between the nucleation and crystallization process in the precursor solution is of significant importance. Therefore, it is necessary to clarify the effects of supersaturation in the space-confined growth.

Furthermore, the space-confined method demonstrates the advantage of substrate-independent characteristics, which facilitate convenient integration of lead-free halide perovskite SCTF

Dr. Z. Q. Li, X. Y. Liu, C. L. Zuo, Dr. W. Yang, Prof. X. S. Fang
Department of Materials Science
Fudan University
Shanghai 200433, P. R. China
E-mail: xshfang@fudan.edu.cn

The ORCID identification number(s) for the author(s) of this article can be found under https://doi.org/10.1002/adma.202103010.

**ADVANCED
SCIENCE NEWS**
www.advancedsciencenews.com

**ADVANCED
MATERIALS**
www.advmat.de

with desired substrates.[8] In this regard, silicon wafer serves as an exceptional platform, due to its mature production fabrication, low cost and complementary performance.[13] The association of perovskite and market-dominant single-crystalline silicon as optoelectronic device is particularly appealing, because this integration may strength the sensitivity of the photodetector to limit value. It is demonstrated that directly integrating organic–inorganic lead halide perovskite $CH_3NH_3PbBr_3$ on silicon wafer makes photodetection range wider and response time shorter.[14] It is also revealed that single-crystal perovskite $CH_3NH_3PbBr_3$ was integrated on silicon wafer for highly sensitive X-ray imaging, through functional molecular bonding between the perovskite and silicon interfaces.[15] In addition, the simple and mild-condition fabrication process of perovskite SCTF gives rise to the possibility of achieving large-area and planar photodetectors at low cost.[16] In particular, metal halide perovskite single crystal can be grown under solution condition and low temperature, and this is ideally compatible with silicon technology without further destroying the wafers. More importantly, the monolithical integration will not only simplify device construction, but also exploit the complementary features to expand some new functionalities.[17]

This paper first demonstrates the in situ observation and growth kinetics of the lead-free perovskite SCTF crystallization. Through supersaturation-controlled space-confined method, a fast-speed and high-sensitivity heterojunction photodetector is fabricated, based on the monolithical integration of $Cs_3Bi_2I_9$ SCTF and silicon substrate. The fast response time and enhanced sensitivity of the photodetector are mainly due to the low lattice mismatch and good band alignment between Si(111) and $Cs_3Bi_2I_9$(001) facets. The results show that the lead-free halide perovskite SCTF with favorable crystal orientation can be directly integrated on silicon wafers to establish high-performance photodetector. This integration provides a feasible strategy to improve the figure of merits of the photodetector and meet the practical requirements of integrated thin-film transistors.

2. Results and Discussion

In the solution system, the crystal growth rate is controlled by the deposition rate and diffusion rate.[18] When the diffusion rate is higher than the deposition rate, the slow deposition may induce twin crystal or polycrystal. In order to avoid the crystallization imperfections caused by high solute diffusion rate, the growth temperature was controlled under 60 °C to realize efficient evaporation. Higher growth temperature can actually increase the evaporation rate of the solvent, however, the obvious cracks were also observed even in small pieces with several hundreds of micrometers (Figure S12, Supporting Information). Additionally, considering the higher boiling temperature, more sensitive solubility and poorer infiltration of γ-butyrolactone (GBL) compared with N,N-dimethylformamide (DMF), the solvent GBL is adopted to achieve the optimal solvent evaporation to attain larger SCTF size, as shown in Figure S13 (Supporting Information). Further, Octadecyltrichlorosilane (OTS) is introduced to prepare the hydrophobic surface of the cover substrate, which effectively minimizes the nucleation

density, reduces the interaction between solvent and substrate, and improves the ion diffusion rate to facilitate continuous large-area growth of the SCTF.[11]

To interpret the growth mechanism of SCTF, in situ observation of the growth process of $Cs_3Bi_2I_9$ SCTF was recorded. **Figure 1**a–d exhibits the real-time growth observations for S25, S35, S45, S55 (S25 represents the saturated solutions prepared at 25°C). $Cs_3Bi_2I_9$ SCTF shows regular hexagon morphology, and the growth rates along the X, Y, and Z directions are close to each other, making the shape constantly keep regular. With the supersaturation of the precursor saturated solution decreasing, the initial nucleation and growth rate are slowed down. The characteristics of the effect of supersaturation on the SCTF growth can be seen more clearly in the Figure 1e, demonstrating the length and area as a function of growth time for S25, S35, S45, S55. For the growth of S25, the curve shows a sharp slope at the beginning and almost reaches a plateau, while the growth rate of $Cs_3Bi_2I_9$ SCTF gradually increases for the low-supersaturation S55 growth. This growth stage is more close to ideal solution system, which can be simulated by single-crystal growth model.

As shown in Figure 1f, the solubility of $Cs_3Bi_2I_9$ in the GBL solvent was measured as a function of temperature. In the temperature range of 15–65 °C, the solubility of $Cs_3Bi_2I_9$ decreases first greatly and then slowly, with the temperature rising up. In the supersaturated zone above the solubility curve, the nucleation barrier height should be overcome to realize the effective spontaneous nucleation and crystallization. Based on classical nucleation theory (details in Supporting Information),[19] the critical nucleus radius r_c, the critical Gibbs free energy change ΔG_c and the chemical potential difference $\Delta\mu$ upon the nucleation formation is expressed as

$$r_C = \frac{2\sigma v_1}{\Delta\mu} \tag{1}$$

$$\Delta G_C = \frac{4\pi}{3}\sigma r_C^2 \tag{2}$$

$$\Delta\mu = \kappa_B T \ln\frac{C}{C_0} \tag{3}$$

As shown in Figure 1g, when the supersaturation of the solution increases from the saturated solution S55 to S25, the nucleation radius r_C decreases, the nucleation barrier decreases. Therefore, the crystallization driving force becomes larger, which is conducive to anti-temperature nucleation. On the other hand, the steady-state nucleation rate J, which is defined as the number of crystal nucleus formed per unit volume per unit time,[19] can be expressed by the Arrhenius reaction rate equation

$$J = A\exp\left(-\frac{\Delta G_C}{k_B T}\right) \tag{4}$$

When the supersaturation reaches a critical value α_c, the nucleation rate J greatly reached to a high value, leading to large amounts of nucleus and destruction of solution system metastability. As shown in Figure S2 (Supporting Information), the
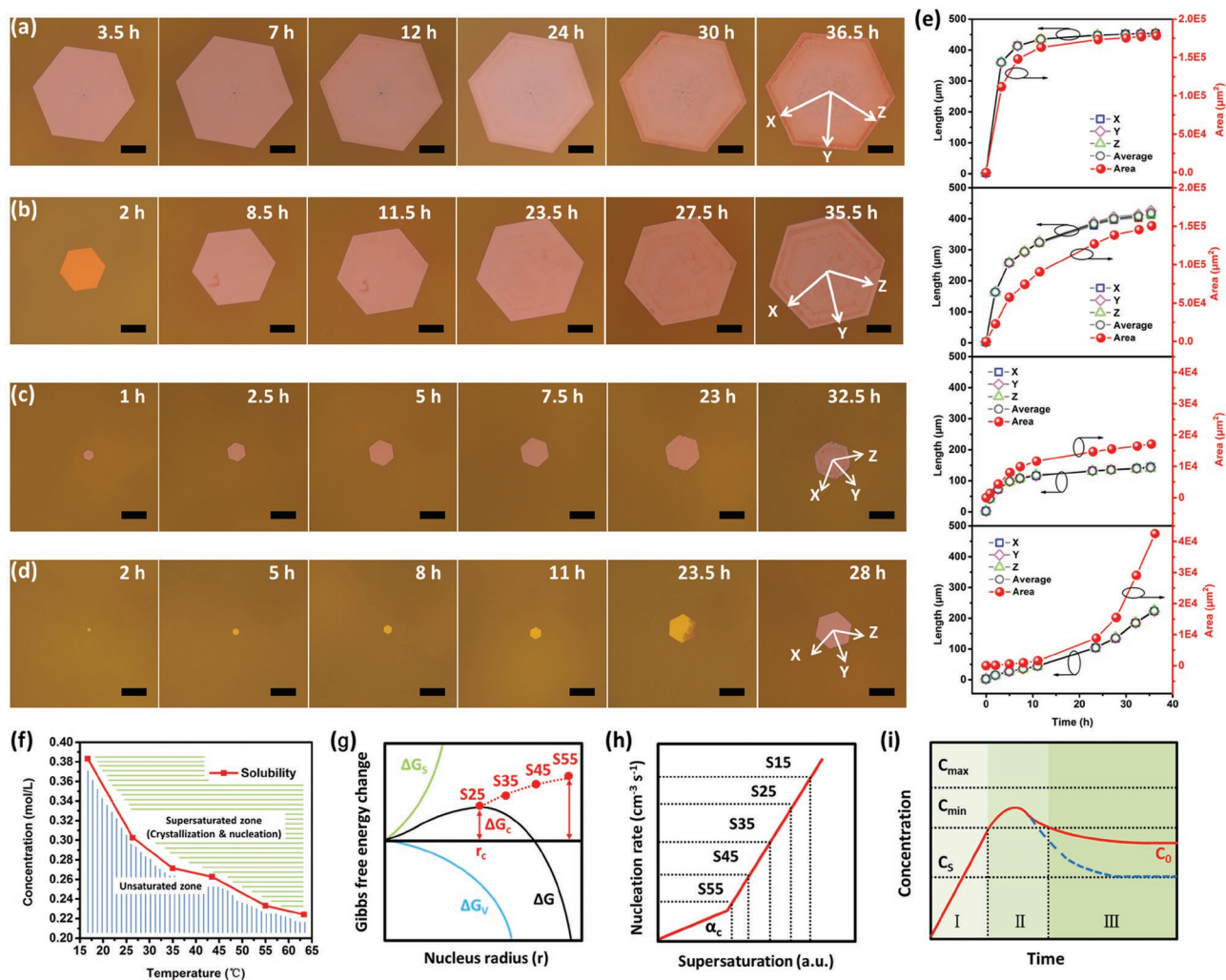
**ADVANCED
SCIENCE NEWS**

www.advancedsciencenews.com

**ADVANCED
MATERIALS**

www.advmat.de

Figure 1. In situ observation and growth kinetics of $Cs_3Bi_2I_9$ SCTF growth. a–d) Real-time growth observations for S25, S35, S45, S55, respectively. (Here, S25 represents the saturated solutions prepared at 25°C). Scale bar: 100 μm. e) The length and area as a function of growth time for S25, S35, S45, S55 (from top to bottom). f) Solubility as a function of temperature. g) The effect of different supersaturation on Gibbs free energy change and critical nucleus radius for homogeneous nucleation. h) Illustration of different supersaturation on the crystal nucleation rate. i) Illustration of the solution concentration as a function of time before and after nucleation. The blue line represents the actual concentration variation.

nucleation density obviously increases from S55 to S15, the saturated solution S15 fails to generate sub-millimeter size SCTF due to excessively high supersaturation. Therefore, controlling the solution supersaturation is utilized to suppress the random nucleation and increase the crystallization driving force.

As shown in Figure 1i, the LaMer model is utilized to demonstrate the nucleation process of the solution system.[10] This process can be divided into three main stages, including pre-nucleation, nucleation and maximum supersaturation. At first, with the solution temperature rising to 60 °C, there will be no apparent nucleation even the concentration exceeds the solubility level. Secondly, when the critical minimum level C_{min} continues to shift down until the solution concentration exceeds the critical minimum level, afterward the nucleation take places. Thirdly, when the critical maximum level C_{max} continues to shift close to the solution concentration, the nucleation rate greatly accelerates with a balanced accumulation and consumption of perovskite monomers. With the consumption

of solutes for continuous growth, the growth process will be terminated as the solution concentration reaches close to the solubility level. In this case, the concentration reduction is delayed and considered to be nearly a constant by the solvent evaporation, leading to the practical concentration curve higher than the solubility curve as a function of time. It is inferred that the growth process of SCTF involves two stages,[20] including the inverse-temperature nucleation and the vaporation growth modeled by two equations (details in Supporting Information)

$$\frac{dm_S}{dt} = -\frac{1}{2}VM_{Cs_3Bi_2I_9}\frac{dC}{dt} \tag{5}$$

$$\frac{dm_S}{dt} = -\frac{1}{2}CM_{Cs_3Bi_2I_9}\frac{dV}{dt} \tag{6}$$

At the initial stage of the inverse-temperature nucleation, the solution volume is thought to be a constant due to insufficient

ADVANCED
SCIENCE NEWS
www.advancedsciencenews.com

ADVANCED
MATERIALS
www.advmat.de

evaporation, and it is the inverse-temperature driving force that play the key role in overcoming the barrier height for nucleation. This result can be supported by the fast nucleation and growth in S25 saturated solution (Figure 1e). At the second stage of the evaporation growth, the solvent reduction keeps the solution concentration unchanged in the continuous growth zone. This result can be supported by the significant increase of the growth rate upon the time in Figure 1e (S55 saturated solution). In fact, the growth of space-confined SCTF is the consequence of the synergistic effect of inverse-temperature crystallization and solvent evaporation, supported by the growth curve evolution from S25 to S55. It is concluded that the saturated solutions S45 realize a balance between nucleation rate and crystallization driving force to achieve high-quality and millimeter-sized SCTF.

Figure 2a,b shows the optical photographs of $Cs_3Bi_2I_9$ SCTF on silicon and glass substrates, and the hexagonal morphology and smooth surface are clearly visible with external size up to 1.5 mm. The color difference is attributed to the different transparency of the substrates. Figure 2c exhibits the XRD pattern of $Cs_3Bi_2I_9$ SCTF, in which the series of strong diffraction peaks at 8.3°, 16.7°, 25.1°, 42.6°, 51.6°, 61.1°, 81.7° belong to {002} crystal planes, according to the standard PDF card No.04-008-8708. Combining high-resolution TEM images (Figure 5d,f) and optical absorption spectrum (Figure S15, Supporting Information), it is proved that the single crystal belongs to dimer polymorph (space group $P6_3/mmc$) rather than layered form (space group $P\overline{3}m1$).[21] These results indicate the high crystalline quality and phase purity for $Cs_3Bi_2I_9$ SCTF, with the crystallographic c direction vertical to the substrate. To precisely investigate the crystallinity of $Cs_3Bi_2I_9$
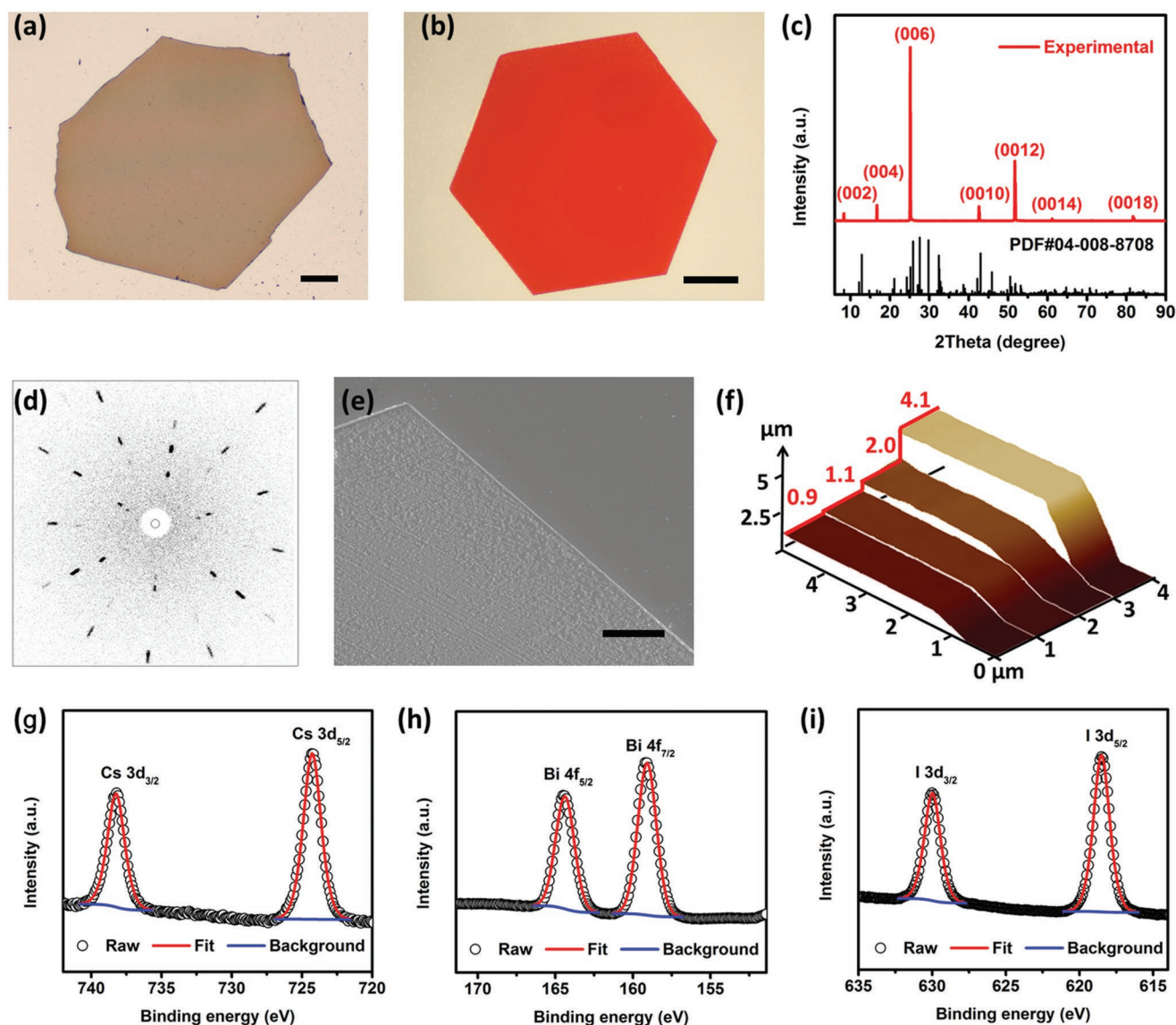

Figure 2. a,b) Characterization of the $Cs_3Bi_2I_9$ SCTF. Optical photographs of $Cs_3Bi_2I_9$ SCTF on Si(111) (a) and glass (b) substrates. The scale bar is 200 µm. c) X-ray diffraction pattern of $Cs_3Bi_2I_9$ SCTF. d) Laue back-reflection pattern of $Cs_3Bi_2I_9$ SCTF. e) SEM image of $Cs_3Bi_2I_9$ SCTF with scale bar: 20 µm. f) 3D AFM images of $Cs_3Bi_2I_9$ SCTF with various thicknesses. g–i) High-resolution XPS for Cs 3d core level (g), Bi 4f core level (h), and I 3d core level (i).

ADVANCED
SCIENCE NEWS
www.advancedsciencenews.com

ADVANCED
MATERIALS
www.advmat.de

SCTF, the Laue back-reflection characterization is adopted to test several positions,[22] as shown in Figure 2d and Figure S4 (Supporting Information). The apparent Laue back-reflection patterns at different points of the $Cs_3Bi_2I_9$ SCTF are clear, bright and uniform with obvious six times symmetry, which is corresponding to the symmetry of $Cs_3Bi_2I_9$ single crystal. This result supports the high crystallinity of the $Cs_3Bi_2I_9$ SCTF, which is sufficient to conduct the evaluations of the photoelectric performances. Figure 2e demonstrates the SEM pattern of the $Cs_3Bi_2I_9$ SCTF free of grain boundaries, in which clear and smooth boundary can be seen even under high magnification. Figure 2f demonstrates the 3D AFM images of $Cs_3Bi_2I_9$ SCTF with various thicknesses. The thickness of the $Cs_3Bi_2I_9$ SCTF can be tuned from 4.1 to 0.9 μm through adjustable pressures. Therefore, an aspect ratio up to 1666 is obtained, and this value is higher than that reported in the literature. [23] As shown in Figure S5 (Supporting Information), the survey XPS exhibits that all peaks are assigned to main constituent elements of the $Cs_3Bi_2I_9$ SCTF. Figure 2g–i

demonstrates the high-resolution XPS patterns for Cs 3d core level, Bi 4f core level and I 3d core level, which are doublet peaks with the spin-orbit coupling separation of 14.0, 5.3, and 11.5 eV, respectively. Cs $3d_{5/2}$, Bi $4f_{7/2}$, I $3d_{5/2}$ core levels locate at 724.2, 159.1, and 618.5 eV, respectively. These parameters indicate the monovalent state for Cs, I elements and trivalent state for Bi element without other oxidation states.[24]

Through the supersaturation-controlled growth, the $Cs_3Bi_2I_9$ (CBI) SCTF is directly integrated on several substrates, including glass, ITO, FTO–TiO_2, ZnO, and Si(111) wafer substrates. The photoelectric performances of these integration photodetectors are investigated systematically, as shown in **Figure 3**. Figure 3a describes the symmetric I–V curves of the dark current and photocurrent for Au–CBI–Au horizontal device, under 350–550 nm illumination. Upon 450 nm illumination and 3 V bias voltage, the photocurrent of SCTF is improved by 30 times than that of polycrystalline thin film (Figure S8, Supporting Information), which benefits from
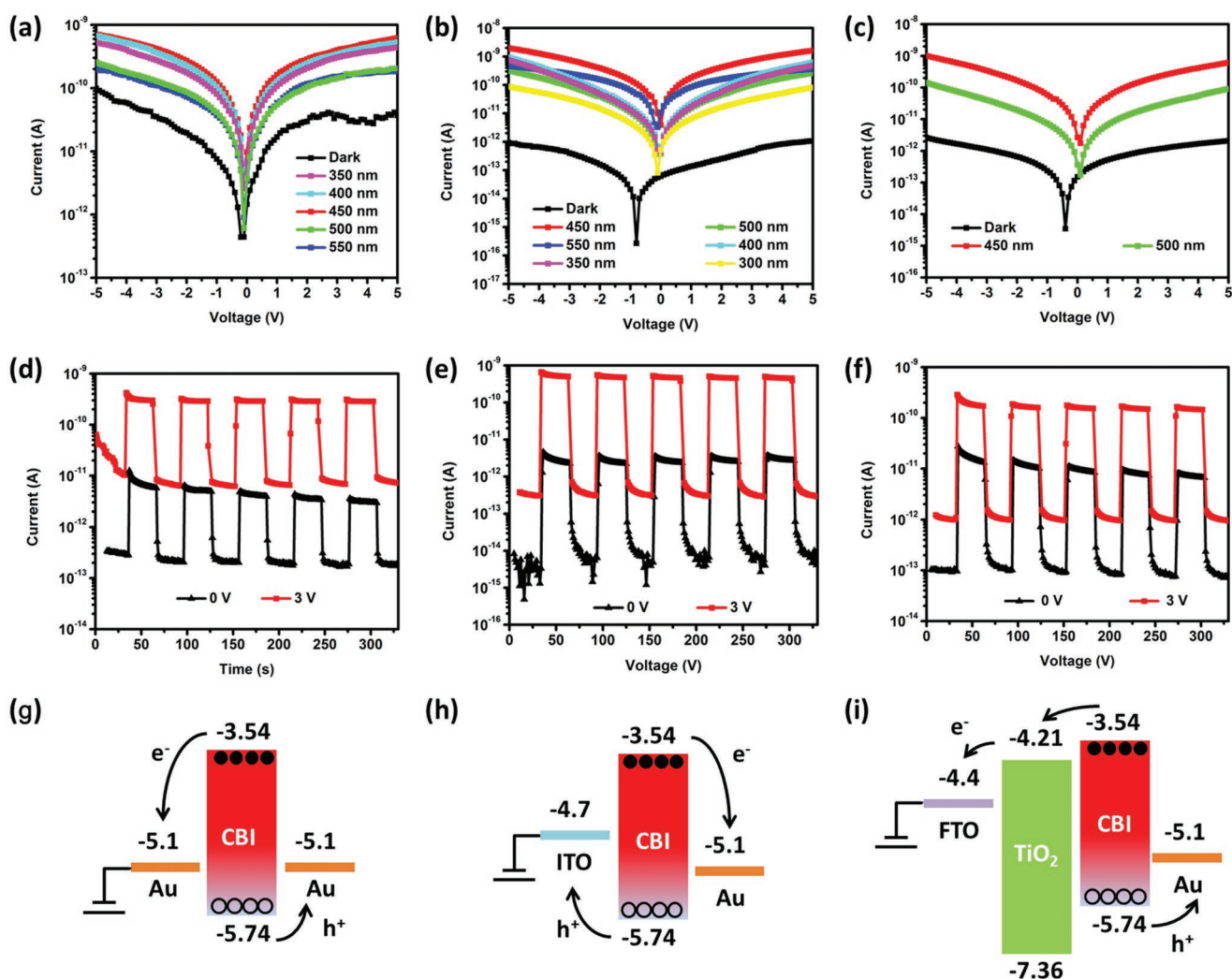

Figure 3. Photoelectric performance of $Cs_3Bi_2I_9$ SCTF on various substrates. a–c) Semilogarithmic I–V curves under dark conditions and illumination of $Cs_3Bi_2I_9$ SCTF on glass, ITO, and FTO–TiO_2 substrates, respectively. d–f) Semilogarithmic I–t curves under 450 nm illumination on/off switching at 0 and 3 V of $Cs_3Bi_2I_9$ SCTF on glass, ITO, and FTO–TiO_2 substrates, respectively. g–i) Schematic illustration of the band alignment of $Cs_3Bi_2I_9$ SCTF on glass, ITO, and FTO–TiO_2 substrates, respectively.

**ADVANCED
SCIENCE NEWS**
www.advancedsciencenews.com

**ADVANCED
MATERIALS**
www.advmat.de

better carrier transport. The deviation of the lowest current from the 0 V voltage is caused by the unbalanced Ag electrodes with unequal sizes for $Cs_3Bi_2I_9$ polycrystalline thin films. The utilization of symmetric Au electrodes construct a nearly ohmic contact with $Cs_3Bi_2I_9$ SCTF under the illumination, which is confirmed by the linear feature for I–V curves in Figure S9 (Supporting Information). In comparison, the ITO–CBI–Au and FTO–TiO_2–CBI–Au devices in Figure 3b,c show Schottky contacts in the dark and illumination, as shown in Figure S9 (Supporting Information). Benefiting from the short carrier transport channel, these vertical devices with asymmetric electrodes demonstrate lower dark current and enhanced on–off ratio compared with Au–CBI–Au horizontal device. All devices demonstrate repeatable and stable photoresponses under 450 nm illumination on/off switching cycles, as shown in Figure 3d–f. These three devices show obvious self-powered performances with ultralow dark current of 0.01 pA and photocurrent of 10 pA, after removing external voltage bias. At 3 V bias, the devices yield dark currents near 1 pA and photocurrent close to 1 nA, with switch ratio up to around 1000.

The good photoelectric performances of the CBI integration photodetectors derive from the band alignment between the CBI and electrodes, leading to effective separation of photogenerated electrons and holes, as shown in Figure 3g–i. In addition, the thin n-type TiO_2 layer with tens of nanometers is served as an electron transport layer for efficient photoelectric responses. The improved switch ratio of the asymmetric device is ascribed to stronger Schottky junction after using ITO and FTO electrodes. The strong Schottky junction, causing the free carriers drifting out of the electrode-semiconductor interface, is utilized to form depletion region and built-in electric field, which provides driving force to separate and collect photogenerated carriers. Furthermore, the successful direct integration of $Cs_3Bi_2I_9$ SCTF on ZnO single crystal also supports the feasibility of supersaturation-controlled space-limited growth. Figure S6 (Supporting Information) demonstrates greatly suppressed dark current and enhanced static switch ratio (up to 100 000) at the negative bias voltage in CBI–ZnO device. It is noted that the large rectification effect results from not only the effective type-II band alignment, but also the closeness of hexagonal crystal structure between the CBI (001) and ZnO (001) facets.

To further facilitate the photoelectric performance of CBI integrated photodetectors, the mature Si(111) wafer was used to combine with lead-free perovskite $Cs_3Bi_2I_9$ SCTF, considering the hexagonal crystal structure of Si(111) facet. **Figure 4**a demonstrates the schematic diagram of the Ag–Si–CBI–Au photodetector. Figure 4b shows the top view of the photodetector. During the steady state photoelectric tests, the Xe lamp was introduced as the light source, with the photodensity as a function of wavelength shown in Figure S10 (Supporting Information). Figure 4c exhibits the semilogarithmic I–V curves of the photodetector under the dark condition and illumination circumstances. I–V curve in the dark condition shows obvious rectifying characteristics, due to the formed heterojunction between silicon and $Cs_3Bi_2I_9$ SCTF interface. Figure 3d shows the semilogarithmic I–t curves under 450 nm illumination, and the stable on–off switching cycles at various bias voltages indicate the repeatable photoresponses of the Si–CBI photodetector.

It is noted that the photoelectric performance is boosted in this device, with the switch ratio up to 3000 and photocurrent close to 10 nA at 3 V bias. The photocurrent and switch ratio of $Cs_3Bi_2I_9$-based photodetectors with different material crystalline form and device type are summarized in **Table 1**. These typical parameters are obviously higher than those of other $Cs_3Bi_2I_9$ SCTF integrated devices in this work.

The photocurrent can be depicted as the function of photodensity at a fixing bias voltage and light wavelength, owing to proportional relationship between the photoinduced carrier generation probability and the absorbed photon flux. Figure 4e demonstrates the steadily decreasing photoresponses under 450 nm illumination and fixing 3 V bias, with decreasing photodensity from 2855 to 12.5 µW cm^{-2}. Figure 4f displays the linearity feature of the logarithmic photodensity-photocurrent curves, indicating a large linear dynamic range for Si–CBI and ITO–CBI photodetectors. After fitting the curve data based on the power equation $I = \alpha P^\theta$ where α represents a constant under fixed wavelength and bias voltage, and θ is calculated to be 0.47 and 0.94 for Si–CBI and ITO–CBI photodetectors. It is suggested that the nonunity exponent θ implies a complex process consisting of free-carriers' generation, transfer, trapping and recombination for the $Cs_3Bi_2I_9$-based photodetector, and the photocurrent of the ITO–CBI photodetector is more sensitive than that of the Si–CBI photodetector.

To access the quality of the photodetectors, responsivity (R_λ), detectivity (D^*) and external quantum efficiency (EQE) are introduced to evaluate the sensitivity, signal-to-noise ratio and photoelectric conversion efficiency of the sensor,[25] whose equations are expressed as

$$R_\lambda = \frac{I_{ph} - I_{dark}}{P_\lambda S} \tag{7}$$

$$D^* = \frac{R_\lambda}{\left(2eI_{dark}/S\right)^{1/2}} \tag{8}$$

$$EQE = \frac{hc}{e}\frac{R_\lambda}{\lambda} \tag{9}$$

where e, h, c represent the elementary charge, Plank constant and the light velocity, considering the illumination wavelength (λ), light power density (P_λ), photocurrent (I_{ph}), dark current (I_{dark}), and effective illumination area (S) of the photodetector. Here, the D^* value may be overestimated through the inferred dark current and responsivity.[12] In general, a low dark current leads to a low noise current. It is noted that the resistivity of the $Cs_3Bi_2I_9$ single crystal is at least two orders of magnitudes higher than $MAPbBr_3$ and other lead-based perovskites. The high resistivity is helpful to reduce background current noise, and the $Cs_3Bi_2I_9$ single-crystal photodetector has a low noise current and high detectivity.[12] Figure 4g–i demonstrate the responsivity, detectivity and EQE as a function of wavelength for Ag–Si–CBI–Au, ITO–CBI–Au and Au–CBI–Au photodetectors. It is common that the peak value is located at 450 or 460 nm and then drops sharply for the $Cs_3Bi_2I_9$-based photodetector, due to the decrease of light absorption of the middle bandgap semiconductor, as shown in Figure S15 (Supporting Information). Unfortunately, the detectivity is limited by the
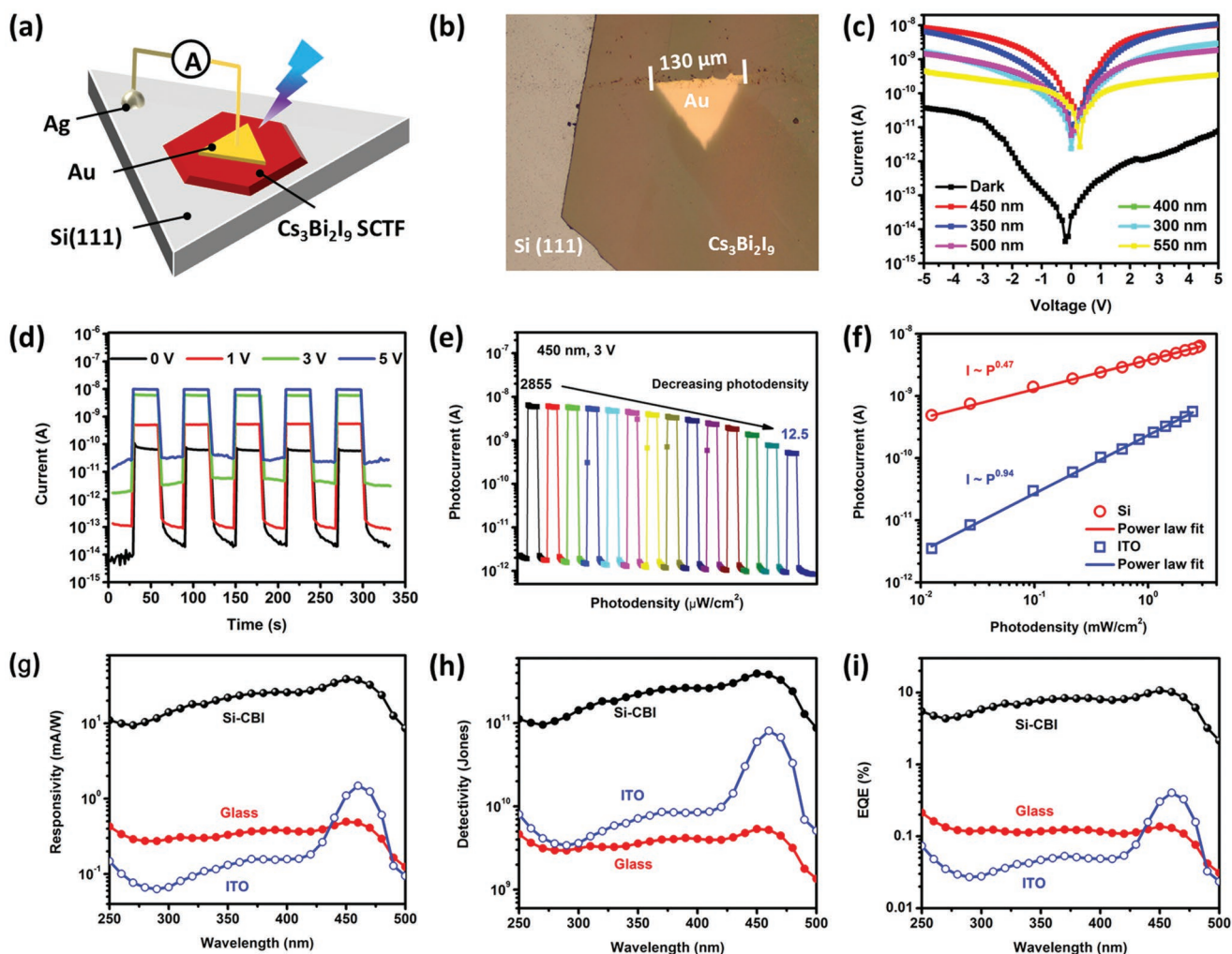
**ADVANCED
SCIENCE NEWS**

www.advancedsciencenews.com

**ADVANCED
MATERIALS**

www.advmat.de

Figure 4. Photoelectric performance of $Cs_3Bi_2I_9$ SCTF on Si(111) substrate. a) Schematic illustration of the Si–CBI photodetector. b) Optical image of the Si–CBI photodetector. c) Semilogarithmic I–V curves under dark condition and illumination of Si–CBI photodetector. d) Semilogarithmic I–t curves under 450 nm illumination on/off switching at various voltages of Si–CBI photodetector. e) Semilogarithmic I–t curve under 450 nm illumination on/off switching at 3 V and various photodensities. f) Photocurrent as a function of photodensity for Si–CBI and ITO–CBI photodetectors. g) Responsivity curves as a function of wavelength for Si–CBI, ITO–CBI and glass-CBI photodetectors. h) Detectivity curves as a function of wavelength for Si–CBI, ITO–CBI and glass-CBI photodetectors. i) EQE curves as a function of wavelength for Si–CBI, ITO–CBI and glass–CBI photodetectors.

relatively weak carrier conductivity, comparing with the most Pb-based perovskites. Several strategies are expected to strength detectivity of the lead-free halide perovskite photodetectors for ensuring potential application, including improving crystal-line quality, adjusting film thickness, surface modification, enhancing light absorption, optimizing device structure and coupling with other photosensitive semiconductors.[4,26–28] Notably, it is apparent that the monolithically integrated

Table 1. Summary of the photocurrent and switching ratio of $Cs_3Bi_2I_9$-based photodetectors with different crystalline form and device type, under 450 nm illumination and 0 V or 3 V bias voltage.

Photodetector	Material	Type	0 V bias		3 V bias	
			Photocurrent [nA]	Switch ratio [a.u.]	Photocurrent [nA]	Switch ratio [a.u.]
Ag–CBI–Ag	PCTF[a]	H[b]	–	–	0.01	10
Au–CBI–Au	SCTF	H	0.007	25	0.3	30
ITO–CBI–Au	SCTF	V	0.002	250	0.6	1000
FTO–TiO_2–CBI–Au	SCTF	V	0.01	100	0.2	200
Ag–Si–CBI–Au	SCTF	V	0.07	3500	8	3000

[a]PCTF represents polycrystalline thin film; [b]H represents the horizontal device structure. V represents the vertical device structure.
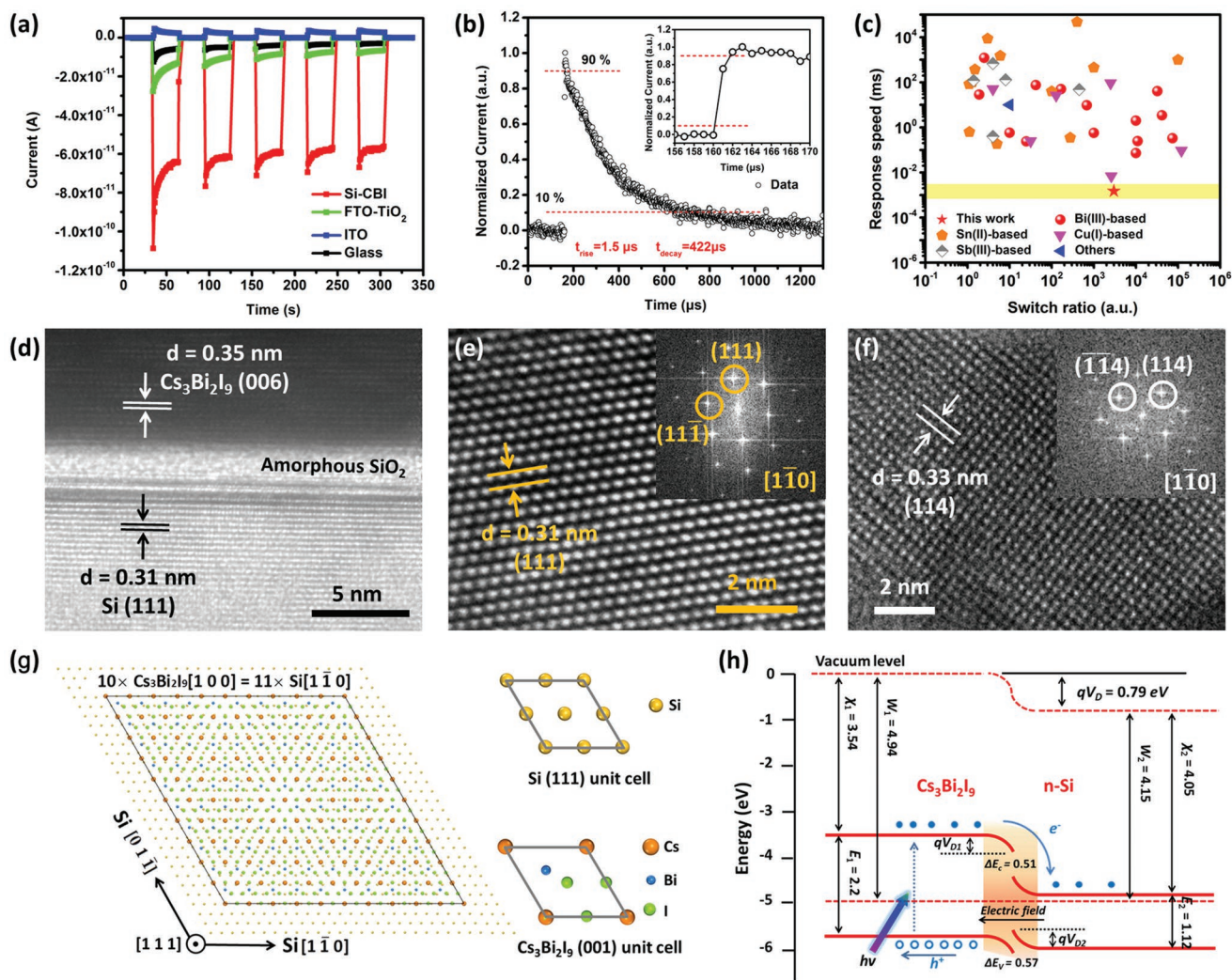
**ADVANCED
SCIENCE NEWS**

www.advancedsciencenews.com

**ADVANCED
MATERIALS**

www.advmat.de

Figure 5. a) Comparison of self-powered performances of Si–CBI, ITO–CBI, FTO–TiO$_2$–CBI, and glass–CBI photodetectors. b) Estimated rise and decay time from photoresponse to 355 nm laser pulse at 3 V bias; the inset is the enlarged curve. c) Response time and switching ratio of the Si–CBI photodetector and reported reference photodetectors. The reference data are from Table S1 (Supporting Information). d) High-resolution TEM image of the cross-section of the contacting interface between Cs$_3$Bi$_2$I$_9$ SCTF and Si(111) wafer. e) High-resolution TEM image of the Si wafer along the $[1\bar{1}0]$ zone axis. f) High-resolution TEM image of Cs$_3$Bi$_2$I$_9$ SCTF along the $[1\bar{1}0]$ zone axis. g) Schematic illustration of lattice match between Si(111) and Cs$_3$Bi$_2$I$_9$(001). h) Schematic illustration of the band alignment in the Si–CBI photodetector.

Ag–Si–CBI–Au photodetector shows boosted 10–200 times figure-of-merit of responsivity, detectivity and EQE than those of the Cs$_3$Bi$_2$I$_9$ SCTF integrated on ITO or glass.

Compared with ITO–CBI, FTO–TiO$_2$–CBI and glass–CBI photodetectors, the great improvement in photoelectric performance can also be confirmed by the enhanced self-powered performance of Si–CBI photodetector, as shown in **Figure 5**a. The self-powered positive photoresponse of ITO–CBI results from the injection of holes into the source terminal, while the negative photoresponses of other devices result from the injection of electrons into the source terminal, as shown in Figure 3g–i. To test the photoresponse time of the photodetector, the transient photoresponse of the Si–CBI photodetector is performed under 355 nm pulse laser at 3 V bias. Figure 5b demonstrates that the rise and decay time of photoresponse, which are estimated to be 1.5 and 422 µs, respectively. Response time and switch ratio

of the Si–CBI photodetector and those reported lead-free halide perovskite photodetectors are compared in Figure 5c. Notably, the photoresponse times of lead-free halide perovskites, which suffer from low switch ratio below 1000, are mostly at the order of microseconds. More importantly, the response speed of this device is likely to be faster, because its peak response is located at the visible light of about 450 nm. These predominant performances, including short response time, high switch ratio and moderate sensitivity, can provide an opportunity for practical high-speed monolithically integrated circuits. It is difficult to conduct TEM measurement, because the ultrasonic process is prone to damage the morphology and single-crystal structure of Cs$_3$Bi$_2$I$_9$ SCTF itself. Focused-ion beam (FIB) prepared Si-CBI samples were utilized to display the original crystal structure of the contacting interface. As shown in Figure 5d, the contacting interface is clearly observed, and its interplanar spacing

is 0.35 and 0.31 nm, corresponding to $Cs_3Bi_2I_9$(006) and Si(111) crystal planes, respectively. These results demonstrate the contacting interface is parallel to $Cs_3Bi_2I_9$(001) facets and Si(111) crystal planes. The layered crystal structure vertical to crystallographic c direction can be clearly observed in $Cs_3Bi_2I_9$ SCTF. The amorphous SiO_2 layer with 2 nm thickness is produced by the oxidation of silicon atoms, and the photogenerated carriers can easily tunnel this layer. Figure 5e displays the high-resolution TEM image of the Si wafer along $[1\bar{1}0]$ zone axis. The crystal lattice fringe can be clearly seen in the high-quality Si single crystal. Figure 5f shows the high-resolution TEM image of $Cs_3Bi_2I_9$ SCTF, and the lattice spacing of 0.33 nm is assigned to the (114) interplanar spacing of $Cs_3Bi_2I_9$ SCTF. Corresponding fast Fourier transform (FFT) analysis of the TEM images was performed along $[1\bar{1}0]$ zone axis, confirming the high-quality crystalline form of $Cs_3Bi_2I_9$ SCTF. It is noted that lead-free halide perovskite $Cs_3Bi_2I_9$ is sensitive to electron beam and suffers from phase transition under high-energy electron beam irradiation. As shown in Figure S14 (Supporting Information), amorphous domain, CsI, BiI_3, and CBI phases were observed after long-term irradiation.

Considering the considerable crystal lattice mismatch between the cubic silicon and hexagonal lead-free halide perovskite $Cs_3Bi_2I_9$, Figure 5g displays the schematic illustration of incommensurate lattice match between the Si(111) crystal plane interfacing with the $Cs_3Bi_2I_9$(001) crystal plane. $Cs_3Bi_2I_9$ possesses the crystal structure of hexagonal phase with $a_1 = b_1 = 8.404$ Å, and the supercell of cubic Si lattice (PDF card No.03-065-1060) along the $[1\bar{1}0]$, $[01\bar{1}]$, [111] axes is hexagonal with $a_2 = b_2 = 7.68$ Å. Although there is a large difference between the lattice constants of the as-grown contacting surfaces for the in-plane periodicities, it is noted that ten unit cells of $Cs_3Bi_2I_9$ match well with eleven unit cells of Si(111) supercell in an incommensurate way, with a relatively low lattice mismatch $f = 0.52\%$ ($f = 1-10a_1/11a_2$). Therefore, it is reasonable that the greatly enhanced photoelectric performance is associated with the highly matched interface with the relationship to be $11 \times$ Si $[1\bar{1}0]$ // $10 \times Cs_3Bi_2I_9$ [100] and $11 \times$ Si $[01\bar{1}]$ // $10 \times Cs_3Bi_2I_9$ [010], according to the above structural analysis. The band alignment of Si–CBI heterojunction photodetector is exhibited in Figure 5h, where the electron affinities (χ) are obtained to be 3.54 and 4.05 eV for $Cs_3Bi_2I_9$ and n-Si, respectively.[29–30] When the p-type $Cs_3Bi_2I_9$ SCTF contacts with n-Si, the depletion region is constructed with transfer of electrons and bending of band structure. The built-in electric field induced by the depletion region promotes the effective separation of photogenerated electrons and holes. The conduction band offset of 0.51 eV facilitates the transfer of photogenerated electrons to the Si side, while the valence band offset of 0.57 eV intercepts the holes on the perovskite side. Although the energy band structure between CBI and silicon actually forms a contact energy barrier rather than a type II heterojunction, the Si–CBI device still shows better performance than other devices. This phenomenon can be partly explained by the importance of lattice matching. When the built-in electric field is weakened by the band structure, there are still advantages in performances including expressed dark current and enhanced photocurrent, due to the good contacting interface. The carrier mobility parameters of lead-free and lead halide perovskites

are provided in the Table S2 (Supporting Information). As we can see, although the carrier mobility of $Cs_3Bi_2I_9$ single crystal is one order of magnitude lower than those of $CsPbBr_3$ and $MAPbI_3$ single crystals, it is comparable to that of $MAPbBr_3$ single crystal and is higher than those of other lead-free halide perovskites. Moreover, the response speed is accelerated by high mobility of single-crystalline CBI material and controllable vertical thickness, which are conducive to electron diffusion and drift, leading to fast separation and collection of photogenerated charges. On the other hand, the lattice matching with silicon can effectively reduce the damage of lattice distortion to the built-in electric field, avoiding the scattering of carriers by the interface defects and the built-in electric field inhomogeneity.

The fast photoresponse mainly results from the effective contacting interface and the high carrier mobility of single-crystalline $Cs_3Bi_2I_9$ and silicon. For p–n heterojunctions, when the donor concentration N_{Si} is far more than the acceptor concentration N_{CBI}, the depletion layer mostly falls in the p-CBI side, and the equations of the depletion layer thickness are given as[31]

$$\frac{X_{Si}}{X_{CBI}} = \frac{N_{CBI}}{N_{Si}} \tag{10}$$

$$X_{Depletion} = X_{CBI} = \sqrt{\frac{2\varepsilon_{CBI}\varepsilon_0 V_D}{eN_{CBI}}} \tag{11}$$

where ε_0 is the vacuum dielectric constant, the relative dielectric constant ε_{CBI} is 4.32, the hole density N_{CBI} is 5.7×10^{12} cm^{-3}, and the contact potential difference V_D is 0.1 V.[4,32] As a result, the depletion layer width is calculated to be 3.0 µm, which is larger than the thickness of CBI SCTF. Because of the relatively thicker depletion layer, the carrier transport is dominated by drift process of the built-in electric field, rather than the diffusion process, resulting in rapid carrier movement. Under illumination, the photogenerated electrons are drifted from CBI side to Si side swiftly, and then are quickly collected by electrodes due to the high electron mobility of silicon. Therefore, controllable vertical thickness and superior lattice match guarantee the improvement of carrier transport in monolithically integrated Si–CBI photodetector.

3. Conclusion

Lead-free halide perovskite $Cs_3Bi_2I_9$ SCTF, with size up to 1.5 mm and thickness from 900 nm to 4.1 µm, was successfully grown via supersaturation-controlled growth method. The nucleation and crystallization kinetics are illustrated through in situ observation of the growth process. It is revealed that the driving force comes from the inverse-temperature nucleation and evaporation crystallization. Typically, saturated solution of 35–45 °C possesses an appropriate supersaturation to balance the nucleation density and growth driving force to obtain high-crystallinity and millimeter-sized SCTF. The phase purity, smooth morphology, crystalline quality, thickness and free of crystal boundary are confirmed. Furthermore, high-quality $Cs_3Bi_2I_9$ SCTF is directly integrated on various substrates, including glass, ITO, FTO–TiO_2, Si(111) wafer, ZnO single crystal. Notably, Ag–Si–CBI–Au photodetector shows boosted 10–200

ADVANCED
SCIENCE NEWS
www.advancedsciencenews.com

ADVANCED
MATERIALS
www.advmat.de

times photoelectric sensitivity, compared with other integrated $Cs_3Bi_2I_9$ SCTF devices. The outstanding performance consists of fast photoresponse time of 1.5 µs and high switch ratio up to 3000, which outperform most of reported lead-free halide perovskite photodetectors. More importantly, mechanism of the photoelectric enhancement is ascribed to low lattice mismatch (only 0.52%) and good band alignment between p-$Cs_3Bi_2I_9$(001) SCTF and n-Si(111) interfaces. The built-in electric field and high-quality crystallinity provide the Si–CBI photodetector with effective separation and fast transfer of photogenerated carriers. It is believed that this work not only provides an insight of the supersaturation in the perovskite precursor chemistry, but also paves the way for direct integration of lead-free halide perovskite with mature silicon industry to fabricate monolithically integrated and high-performance photodetectors.

Supporting Information

Supporting Information is available from the Wiley Online Library or from the author.

Conflict of Interest

The authors declare no conflict of interest.

Data Availability Statement

Research data are not shared.

[1] Z. Xiao, Z. Song, Y. Yan, *Adv. Mater.* **2019**, *31*, 1803792.
[2] J. Luo, M. Hu, G. Niu, J. Tang, *ACS Appl. Mater. Interfaces* **2019**, *11*, 31575.
[3] Q. Fan, G. V. Biesold-McGee, J. Ma, Q. Xu, S. Pan, J. Peng, Z. Lin, *Angew. Chem., Int. Ed.* **2020**, *59*, 1030.
[4] F. Cao, L. Li, *Adv. Funct. Mater.* **2021**, *31*, 2008275.
[5] M. Keshavarz, E. Debroye, M. Ottesen, C. Martin, H. Zhang, E. Fron, R. Küchler, J. A. Steele, M. Bremholm, J. Van de Vondel, H. I. Wang, M. Bonn, M. B. J. Roeffaers, S. Wiedmann, J. Hofkens, *Adv. Mater.* **2020**, *32*, 2001878.
[6] Y. Liu, Y. Zhang, X. Zhu, Z. Yang, W. Ke, J. Feng, X. Ren, K. Zhao, M. Liu, M. G. Kanatzidis, S. Liu, *Sci. Adv.* **2021**, *7*, eabc8844.
[7] Y. Liu, Y. Zhang, Z. Yang, D. Yang, X. Ren, L. Pang, S. Liu, *Adv. Mater.* **2016**, *28*, 9204.
[8] Y.-X. Chen, Q.-Q. Ge, Y. Shi, J. Liu, D.-J. Xue, J.-Y. Ma, J. Ding, H.-J. Yan, J.-S. Hu, L.-J. Wan, *J. Am. Chem. Soc.* **2016**, *138*, 16196.
[9] W. Peng, L. Wang, B. Murali, K.-T. Ho, A. Bera, N. Cho, C.-F. Kang, V. M. Burlakov, J. Pan, L. Sinatra, C. Ma, W. Xu, D. Shi, E. Alarousu, A. Goriely, J.-H. He, O. F. Mohammed, T. Wu, O. M. Bakr, *Adv. Mater.* **2016**, *28*, 3383.
[10] M. Jung, S.-G. Ji, G. Kim, S. I. Seok, *Chem. Soc. Rev.* **2019**, *48*, 2011.
[11] Z. Chen, Q. Dong, Y. Liu, C. Bao, Y. Fang, Y. Lin, S. Tang, Q. Wang, X. Xiao, Y. Bai, Y. Deng, J. Huang, *Nat. Commun.* **2017**, *8*, 1890.
[12] Y. Zhang, Y. Liu, Z. Xu, H. Ye, Z. Yang, J. You, M. Liu, Y. He, M. G. Kanatzidis, S. Liu, *Nat. Commun.* **2020**, *11*, 2304.
[13] W. Yang, J. Chen, Y. Zhang, Y. Zhang, J.-H. He, X. S. Fang, *Adv. Funct. Mater.* **2019**, *29*, 1808182.
[14] X. Geng, F. Wang, H. Tian, Q. Feng, H. Zhang, R. Liang, Y. Shen, Z. Ju, G.-Y. Gou, N. Deng, Y.-t. Li, J. Ren, D. Xie, Y. Yang, T.-L. Ren, *ACS Nano* **2020**, *14*, 2860.
[15] W. Wei, Y. Zhang, Q. Xu, H. Wei, Y. Fang, Q. Wang, Y. Deng, T. Li, A. Gruverman, L. Cao, J. Huang, *Nat. Photonics* **2017**, *11*, 315.
[16] M. De Bastiani, A. J. Mirabelli, Y. Hou, F. Gota, E. Aydin, T. G. Allen, J. Troughton, A. S. Subbiah, F. H. Isikgor, J. Liu, L. Xu, B. Chen, E. Van Kerschaver, D. Baran, B. Fraboni, M. F. Salvador, U. W. Paetzold, E. H. Sargent, S. De Wolf, *Nat. Energy* **2021**, *6*, 167.
[17] X.-W. Tong, Z.-X. Zhang, D. Wang, L.-B. Luo, X. Xie, Y.-C. Wu, *J. Mater. Chem. C* **2019**, *7*, 863.
[18] Y. Liu, Y. Zhang, Z. Yang, J. Feng, Z. Xu, Q. Li, M. Hu, H. Ye, X. Zhang, M. Liu, K. Zhao, S. Liu, *Mater. Today* **2019**, *22*, 67.
[19] I. V. Markov, *Crystal Growth for Beginners: Fundamentals of Nucleation, Crystal Growth and Epitaxy*, World Scientific, Singapore **2016**.
[20] Y. Liu, Y. Zhang, Z. Yang, H. Ye, J. Feng, Z. Xu, X. Zhang, R. Munir, J. Liu, P. Zuo, Q. Li, M. Hu, L. Meng, K. Wang, D.-M. Smilgies, G. Zhao, H. Xu, Z. Yang, A. Amassian, J. Li, K. Zhao, S. Liu, *Nat. Commun.* **2018**, *9*, 5302.
[21] S. E. Creutz, H. Liu, M. E. Kaiser, X. Li, D. R. Gamelin, *Chem. Mater.* **2019**, *31*, 4685.
[22] B. C. Larson, W. Yang, G. E. Ice, J. D. Budai, J. Z. Tischler, *Nature* **2002**, *415*, 887.
[23] Z. Yang, Y. Deng, X. Zhang, S. Wang, H. Chen, S. Yang, J. Khurgin, N. X. Fang, X. Zhang, R. Ma, *Adv. Mater.* **2018**, *30*, 1704333.
[24] J. F. Moulder, W. F. Stickle, P. E. Sobol, K. D. Bomben, *Handbook of X-ray Photoelectron Spectroscopy*, Perkin-Elmer, Eden Prairie, MN, USA **1992**.
[25] F. Teng, K. Hu, W. Ouyang, X. S. Fang, *Adv. Mater.* **2018**, *30*, 1706262.
[26] Y. Li, Z. Shi, W. Liang, J. Ma, X. Chen, D. Wu, Y. Tian, X. Li, C. Shan, X. S. Fang, *Mater. Horiz.* **2021**, *8*, 1367.
[27] Z. Q. Li, Z. L. Li, Z. F. Shi, X. S. Fang, *Adv. Funct. Mater.* **2020**, *30*, 2002634.
[28] H. P. Wang, S. Y. Li, X. Y. Liu, Z. F. Shi, X. S. Fang, J. H. He, *Adv. Mater.* **2021**, *33*, 2003309.
[29] B.-B. Yu, M. Liao, J. Yang, W. Chen, Y. Zhu, X. Zhang, T. Duan, W. Yao, S.-H. Wei, Z. He, *J. Mater. Chem.* **2019**, *7*, 8818.
[30] W. Yang, K. Hu, F. Teng, J. Weng, Y. Zhang, X. S. Fang, *Nano Lett.* **2018**, *18*, 4697.
[31] D. A. Neamen, *Semiconductor Physics and Devices: Basic Principles*, McGraw-Hill, New York **2012**.
[32] M. Pazoki, M. B. Johansson, H. Zhu, P. Broqvist, T. Edvinsson, G. Boschloo, E. M. J. Johansson, *J. Phys. Chem. C* **2016**, *120*, 29039.